

Modeling adhesive contacts under mixed-mode loading

Khajeh Salehani, M.; Irani, N.; Nicola, L.

DOI

[10.1016/j.jmps.2019.06.010](https://doi.org/10.1016/j.jmps.2019.06.010)

Publication date

2019

Document Version

Final published version

Published in

Journal of the Mechanics and Physics of Solids

Citation (APA)

Khajeh Salehani, M., Irani, N., & Nicola, L. (2019). Modeling adhesive contacts under mixed-mode loading. *Journal of the Mechanics and Physics of Solids*, 130, 320-329. <https://doi.org/10.1016/j.jmps.2019.06.010>

Important note

To cite this publication, please use the final published version (if applicable).
Please check the document version above.

Copyright

Other than for strictly personal use, it is not permitted to download, forward or distribute the text or part of it, without the consent of the author(s) and/or copyright holder(s), unless the work is under an open content license such as Creative Commons.

Takedown policy

Please contact us and provide details if you believe this document breaches copyrights.
We will remove access to the work immediately and investigate your claim.



Modeling adhesive contacts under mixed-mode loading

M. Khajeh Salehani^{a,*}, N. Irani^a, L. Nicola^{a,b,*}

^a Department of Materials Science and Engineering, Delft University of Technology, CD Delft 2628, the Netherlands

^b Department of Industrial Engineering, University of Padova, Padua 35131, Italy

ARTICLE INFO

Article history:

Received 12 February 2019

Revised 17 June 2019

Accepted 17 June 2019

Available online 18 June 2019

Keywords:

Adhesive contacts

Green's function molecular dynamics

Contact area

Onset of sliding

Reattachment

ABSTRACT

Experiments show that when an adhesive contact is subjected to a tangential load the contact area reduces, symmetrically or asymmetrically, depending on whether the contact is under tension or compression. What happens after the onset of sliding is more difficult to be assessed because conducting experiments is rather complicated, especially under tensile loading. Here, we provide through numerical simulations, a complete picture of how the contact area and tractions of an adhesive circular smooth punch evolve under mixed-mode loading, before and after sliding. First, the Green's function molecular dynamics method is extended to include the description of the interfacial interactions between contacting bodies by means of traction–separation constitutive laws that enforce coupling between tension (or compression) and shear. Next, simulations are performed to model sliding of a circular smooth punch against a flat rigid substrate, under tension and compression. In line with the experimental observations, the reduction in the contact area during shear loading is found to be symmetric under tension and asymmetric under compression. In addition, under tensile loading, full detachment is observed at the onset of sliding with a non-zero value of the tangential force. After the onset of sliding and the occurrence of slip instability, the contact area abruptly increases (reattachment), under both tension and compression. For interfaces with high friction, the reattachment occurs only partially. However, a full reattachment is attainable when friction is low.

© 2019 The Authors. Published by Elsevier Ltd.

This is an open access article under the CC BY-NC-ND license.

(<http://creativecommons.org/licenses/by-nc-nd/4.0/>)

1. Introduction

In the seminal work by Savkoor and Briggs (1977) mixed normal and tangential loading was applied to a rubber hemisphere in adhesive contact with a glass plate. It was found that as a result of increasing the tangential load, the surfaces tend to peel apart and hence, the contact area decreases progressively. Waters and Guduru (2010) performed similar experiments for a wide range of normal loads (tensile and compressive) while continually recording images of the contact area evolution. These images demonstrated a symmetric contact area reduction under tensile loading and an asymmetric reduction under compressive loading, before the onset of sliding. Moreover, they captured a partial reattachment with the advent of slip instability at the interface under compressive loading. However, under tensile loading this reattachment was not observed. Recently, Sahli et al. (2018) carried out experiments on an asperity sliding on a flat plate under compression

* Corresponding authors.

E-mail addresses: m.khajehsalehani@tudelft.nl (M. Khajeh Salehani), l.nicola@tudelft.nl (L. Nicola).

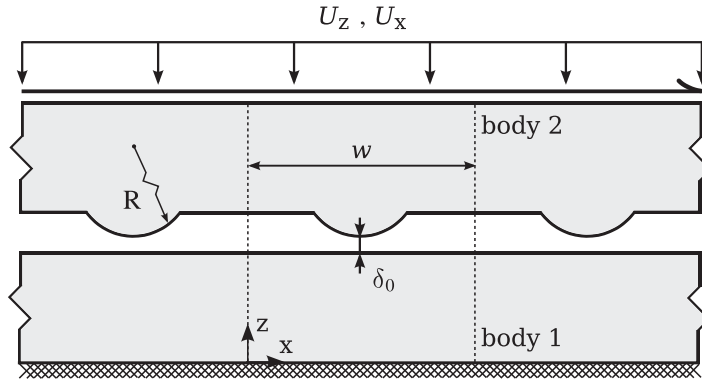


Fig. 1. Sketch of the two-dimensional contact problem.

and found that both smooth and rough asperities follow similar contact area–force equations during shear loading up to the onset of sliding.

The aim of this study is to develop a computational technique to study adhesive frictional contacts under mixed-mode (normal and tangential) loading that can reproduce the features observed in the above-mentioned experiments and predict the contact behavior in conditions that are difficult to be achieved experimentally, i.e. after the onset of sliding. By that we intend to provide a complete picture of the adhesive frictional problem for smooth contacts.

In the past decades, several adhesive contact models such as Johnson–Kendall–Roberts (JKR) [Johnson et al. \(1971\)](#), Derjaguin–Muller–Toporov (DMT) [Derjaguin et al. \(1975\)](#), Maugis–Dugdale (MD) [Maugis \(1992\)](#), and more recently [Greenwood and Johnson \(1998\)](#) and [Barthel and Haiat \(2002\)](#) have been proposed and widely used. However, these models are not applicable if there is tangential loading. Adhesive contacts under mixed-mode loading have been extensively studied in [Savkoor and Briggs \(1977\)](#), [Waters and Guduru \(2010\)](#), [Thornton \(1991\)](#), [Johnson \(1997\)](#), [Chen and Wang \(2006\)](#) and [Ciavarella \(2018\)](#) by using linear elastic fracture mechanics (LEFM) or the modified (mixed-mode) JKR adhesion theory, but these studies tackled exclusively non-slipping contacts. [Adams \(2014\)](#) investigated adhesive contact of elastic cylinders under mixed-mode loading where both stick and slip regions can be present at the interface. Adams' analysis works well for compressive loading, but not for tensile loading: his formulation leads to negative contact sizes. Recently, [Huang and Yan \(2017\)](#) introduced a model for sliding of adhesive contacts with the aim of analysing shearing problems under both compressive and tensile loading. With the same aim, [Mergel et al. \(2018\)](#) developed a continuum contact model based on the finite element method (FEM). However, both works ([Huang and Yan, 2017](#); [Mergel et al., 2018](#)) are limited to study the contact area evolution only up to the onset of sliding.

In this work, the static elastic deformation of the body is modeled using Green's function molecular dynamics (GFMD) ([Khajeh Salehani et al., 2018](#)). The interactions between the surfaces are described through constitutive traction–separation laws, of the type used in cohesive zone models (CZMs). Among the wide class of CZMs ([Van den Bosch et al., 2006](#); [McGarry et al., 2014](#); [Sun et al., 1993](#); [Xu and Needleman, 1993](#)), we have selected the so-called NP1 model proposed by [McGarry et al. \(2014\)](#). The NP1 is a non-potential based CZM, therefore less rigorous in formulation than the potential based models in the literature. However, it has the advantage that it works well both under compression and tension when coupled to shear. More specifically, the physics of overclosure are well captured: the resistance to tangential separation increases with increasing overclosure.

While the presented formulation is applicable to linearly elastic solids with a generic surface roughness obeying the small slope approximation, the focus of our analysis is on the contact shearing of a flat rigid substrate with a deformable solid. First, simulations are performed for flat-on-flat contact shearing to assess the capability of our model to capture the typical stick-slip behavior during sliding ([Dikken et al., 2017](#); [Gao, 2010](#); [Socoliuc et al., 2004](#)). Then, simulation results are presented for the adhesive frictional contact between a deformable circular protrusion and a flat rigid substrate.

2. Method

2.1. Problem formulation

A flat rigid substrate (body 1) is adjacent to an elastically deformable solid (body 2), having periodic circular protrusions with radius R , as schematically shown in [Fig. 1](#). Periodicity is an intrinsic property of the Greens' function molecular dynamics model, which relies on the periodicity of Fourier transforms. In this work, we focus on the behavior of a single protrusion, therefore we take the width of the periodic unit cell w to be large enough to guarantee that the asperity does not interact with its replicas within the range of applied loads.

The bottom boundary of body 1 is fixed. The minimum distance between the bodies is initially δ_0 . A uniform normal displacement U_z^f is then applied at the top boundary of body 2, with the approach displacement defined as $\delta = U_z^f - \delta_0$.

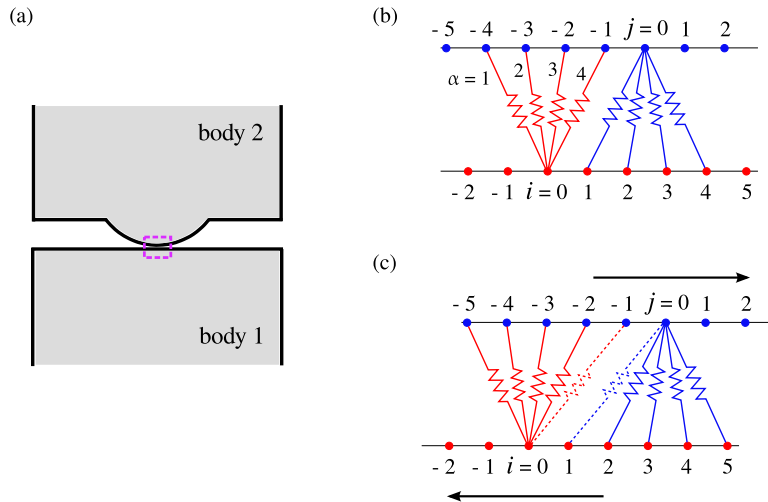


Fig. 2. (a) Schematic representation of the bodies in contact. (b) The interfacial interactions are represented by springs for the region highlighted by a dashed rectangle. (c) The updated set of interaction springs, in a snapshot after sliding.

Next, a uniform tangential displacement U_x is exerted incrementally on the same boundary, while its vertical displacement is constrained.

Body 2 is taken to be elastically isotropic. Plane-strain conditions are assumed for the two-dimensional problem with deformations restricted to the x - z plane (see Fig. 1). The surfaces of the contacting solids are discretized with a number of equispaced nodes. In the GFMD technique, the response of the material to the external load is obtained using damped dynamics by only considering the interactions of the surface nodes with their degrees of freedom coupled to the external force (Prodanov et al., 2014). By taking advantage of the translational symmetry of the problem, the equilibrium solution is obtained numerically in reciprocal space.

In order to keep track of the surface evolution during loading, the calculation is carried out in an incremental manner (Spence, 1968) with the applied load increasing monotonically. For more details on the incremental scheme, the reader is referred to the previous paper by the authors (Khajeh Salehani et al., 2018). Eventually, based on the solution for the surface, body fields are calculated by means of analytical relations (Venugopalan et al., 2017).

2.2. Interfacial interactions

The interfacial interactions are modeled through traction-separation laws. To visualize the interactions between discretized nodes at the interface, we will represent them through “springs”, as sketched in Fig. 2b. Red (or blue) springs represent the interactions between node i (or j) belonging to the surface of a body and the nodes of the opposite surface. Fig. 2c illustrates a snapshot of the same region shown in Fig. 2b after sliding, along with the updated set of interaction springs between the two surfaces. In principle, each node can be connected through springs to all other nodes of the surface of the counter-body. However, to limit the computational cost of the simulation, since the interactions with far away nodes is very weak, we consider that each node reaches out with springs only to the nodes that fall within a window, that moves with the node itself. In Fig. 2c the dashed springs are those that fall outside of the window.

The interface model is implemented in the Green’s function molecular dynamics (GFMD) technique described in Khajeh Salehani et al. (2018) as follows. When the two solids are in mechanical equilibrium at time t , they exchange at the interface equal and opposite forces:

$$\mathbf{T}_{\text{if}}^{(1)} = -\mathbf{T}_{\text{if}}^{(2)} \quad \forall t, \quad (1)$$

where \mathbf{T}_{if} is the interfacial traction. The interfacial tractions acting on each node i are computed as a sum over the m springs in the window:

$$\mathbf{T}_{\text{if}}(i) = \sum_{\alpha}^m \mathbf{T}_{\text{cz}}[\Delta_{\text{t}}(i, \alpha), \Delta_{\text{n}}(i, \alpha)], \quad (2)$$

where \mathbf{T}_{cz} is the constitutive relation of each individual spring as a function of the tangential and normal gap values, i.e., the end-to-end distance of the springs:

$$\begin{aligned} \Delta_{\text{t}}(i, \alpha) &= x(j) - x(i), \\ \Delta_{\text{n}}(i, \alpha) &= z(j) - z(i), \end{aligned} \quad (3)$$

where j refers to each of the m nodes connected through springs to i .

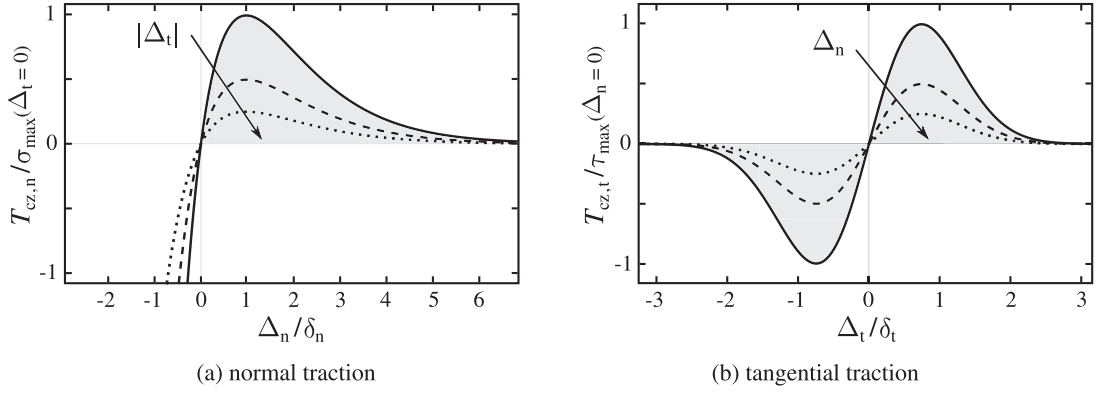


Fig. 3. Graphical representation of normal and tangential tractions versus normal and tangential gap values, as given by the cohesive-zone constitutive relations of Eq. (4).

In this work, T_{Cz} is specified in terms of the cohesive-zone constitutive relations in normal and tangential directions, $T_{Cz,n}$ and $T_{Cz,t}$, which represent the adhesive and frictional forces per unit area, respectively. Following McGarry et al. (2014), the constitutive relations are expressed as

$$T_{Cz,n} = \frac{\phi_n}{\delta_n} \left(\frac{\Delta_n}{\delta_n} \right) \exp \left(-\frac{\Delta_n}{\delta_n} \right) \exp \left(-\frac{\Delta_t^2}{\delta_t^2} \right),$$

$$T_{Cz,t} = 2 \frac{\phi_t}{\delta_t} \left(\frac{\Delta_t}{\delta_t} \right) \exp \left(-\frac{\Delta_n}{\delta_n} \right) \exp \left(-\frac{\Delta_t^2}{\delta_t^2} \right), \tag{4}$$

where (ϕ_n, ϕ_t) and (δ_n, δ_t) are, respectively, the normal and tangential works of separation and characteristic lengths of each individual spring. Consequently, the maximum values of $T_{Cz,n}$ and $T_{Cz,t}$, i.e., the normal and tangential cohesive-zone strengths σ_{max} and τ_{max} , are given as

$$\sigma_{max} = \frac{1}{\exp(1)} \frac{\phi_n}{\delta_n} \exp \left(-\frac{\Delta_t^2}{\delta_t^2} \right),$$

$$\tau_{max} = \frac{1}{\sqrt{0.5 \exp(1)}} \frac{\phi_t}{\delta_t} \exp \left(-\frac{\Delta_n}{\delta_n} \right), \tag{5}$$

as graphically shown in Fig. 3. These relations describe well the interface interaction between common materials (Khajeh Salehani et al., 2018). If desired, it is possible to employ a different “traction-separation” law for modeling other systems, such as biological structures.

2.3. Choice of parameters

The circular protrusion on the surface of body 2 has a radius of $R/w = 2.5$, which is sufficiently large to obey the small slope approximation. The chosen material and interface properties are presented in terms of non-dimensional parameters $\bar{\square} = \square / \square^{ref}$, where the following “reference” parameters are used: $E^{ref} = 1$ GPa, $\phi_n^{ref} = \phi_t^{ref} = 1$ N/m, and $\delta_n^{ref} = \delta_t^{ref} = 1$ nm. The reference parameters are chosen to be unity and are only used for normalization. Unless otherwise specified, $\bar{\delta}_n = \bar{\delta}_t = 1$, $\bar{\phi}_n = 2$, the ratio of tangential-to-normal work of separation $\phi_t / \phi_n = 1$, and $\bar{E} = \bar{E}^{(2)} = 70$. Moreover, $E^{(1)} = 10^3 E^{(2)}$ (body 1 is assumed to be rigid) and $\nu = \nu^{(1)} = \nu^{(2)} = 0.45$. Here, we opt for $\nu = 0.45$ since most of the experiments have been performed for almost incompressible materials.

The initial distance between the two solids is $\delta_0 = 10 \delta_n$, which is large enough to have zero interface interactions at the beginning of the calculations (see Fig. 3a). Simulations are performed for a wide range of normal displacements $\bar{\delta} := \delta / \delta_0 = [-1, 1]$ in order to study both tensile and compressive loading. When considering flat-on-flat contact (no protrusion), we take $\bar{\delta} = 0$, so that $\Delta_n = 0$ all over the interface, providing the opportunity to assess our model in pure-shear mode (see Eq. (4)).

The applied tangential displacement U_x is normalized on the width of the unit cell $\bar{U}_x = U_x / w$. The tangential and normal contact forces are, respectively, calculated as

$$F = \int_0^w T_{if,t}^{(1)} dx = - \int_0^w T_{if,t}^{(2)} dx,$$

$$L = - \int_0^w T_{if,n}^{(1)} dx = \int_0^w T_{if,n}^{(2)} dx, \tag{6}$$

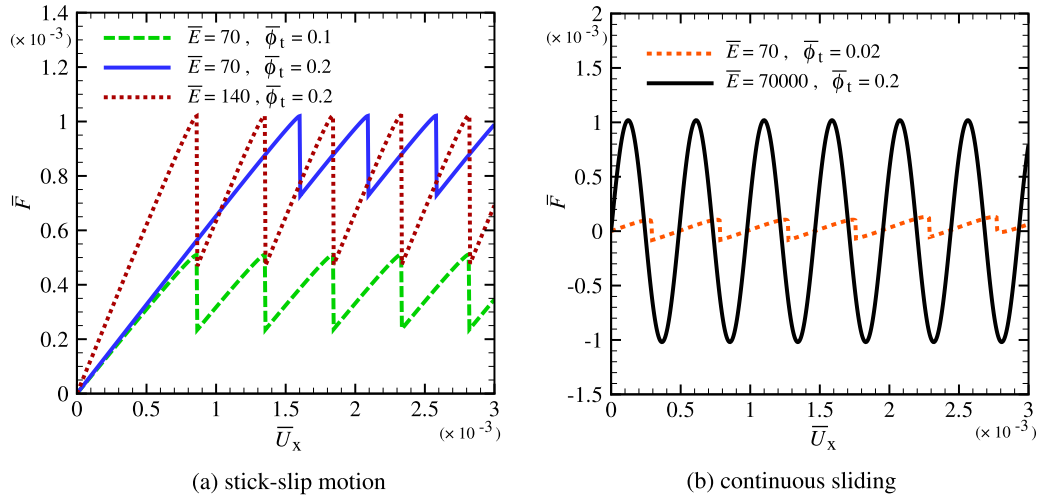


Fig. 4. Tangential contact force \bar{F} versus applied tangential displacement \bar{U}_x for various values of elastic modulus \bar{E} and tangential work of separation $\bar{\phi}_t$. A transition is observed from stick-slip motion (a) to continuous sliding (b) by increasing \bar{E} or decreasing $\bar{\phi}_t$. In all cases, the elastic modulus $\bar{E} = 70$ is used in normalizing the tangential contact force.

where we have considered that the out-of-plane thickness of the solids is unity, and chosen that an attractive normal force is negative. These contact forces are normalized as $\bar{F} = (F/w)/E$ and $\bar{L} = (L/w)/E$. The contact area A is defined as the size of the interface under repulsion and is normalized as $\bar{A} = A/w$.

The numerical convergence is guaranteed by employing an incremental displacement $\Delta U_z = \delta_n/10$ and $\Delta U_x = \delta_t/10$. To make the simulations computationally more efficient, the interaction between two opposite nodes is considered only if they fall within an interaction “window”. The size of this window is independent of the surface discretization and is determined by the range of the cohesive-zone interactions. A converged solution is achieved by setting the window-size to 10 δ_n in normal and 5 δ_t in tangential directions.

3. Results and discussion

3.1. Flat-on-flat contact

Simulations are first performed for flat-on-flat contact under simple shearing to assess the capability of our model to predict the stick-slip motion observed experimentally (Socoliuc et al., 2004), via atomistic simulations (Dikken et al., 2017), and macroscopic models such as Gao (2010). Besides, we observe the transition from stick-slip motion to continuous sliding, where the dissipated energy becomes negligible (Krylov and Frenken, 2014) and hence, an ultra low friction regime can be achieved.

Results for various values of elastic modulus \bar{E} and tangential work of separation $\bar{\phi}_t$ in Fig. 4a indeed show the typical sawtooth behavior (Dikken et al., 2017; Socoliuc et al., 2004) of the tangential contact force \bar{F} versus the applied tangential displacement \bar{U}_x . In all cases, in the initial sticking stage, the force increases linearly with applied tangential displacement, with a slope controlled by \bar{E} . The force then drops abruptly as the two solids slip over each other. For stiffer materials, the stored elastic energy is larger and is released by a larger drop in force at each slip instability. This can be seen by comparing the blue solid line for $\bar{E} = 70$ and the dotted red line for $\bar{E} = 140$ in Fig. 4a. Moreover, as expected, as the interface interactions become weaker (by decreasing the tangential work of separation $\bar{\phi}_t$) the onset of sliding occurs at a lower tangential contact force \bar{F} . This can be observed by comparing the blue solid line for $\bar{\phi}_t = 0.2$ and the dashed green line for $\bar{\phi}_t = 0.1$ in Fig. 4a.

As shown in Fig. 4b, a transition from stick-slip motion to continuous sliding is observed either when $\bar{\phi}_t$ is decreased or when \bar{E} is increased. By continuous sliding we mean that the tangential contact force oscillates around zero with no initial sticking stage. In this case, the dissipated energy during sliding becomes negligible and hence, an ultra low friction regime is achieved. This is in line with the predictions of the Prandtl–Tomlinson model for cases in which the contact potential corrugation is low enough (low $\bar{\phi}_t$ in this work) and/or the stiffness of the system is high enough (high \bar{E} in this work) (Krylov and Frenken, 2014).

Here, the friction force (\bar{F}) is calculated as the average of the maximum and the minimum tangential contact force during sliding (Krylov and Frenken, 2014), \bar{F}_s and \bar{F}_k :

$$\langle \bar{F} \rangle = \frac{\bar{F}_s + \bar{F}_k}{2}. \quad (7)$$

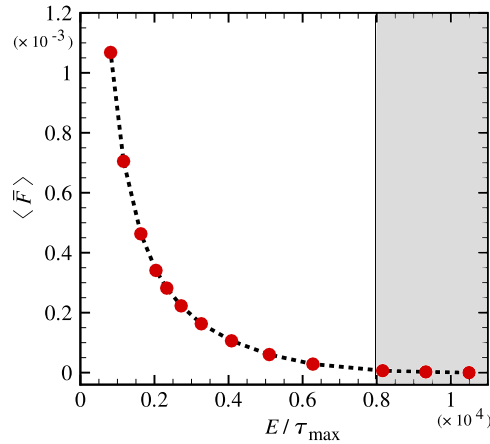


Fig. 5. Friction reduces by increasing E/τ_{\max} . The shaded area indicates the ultra low friction regime. The dashed line is a guide for the eye.

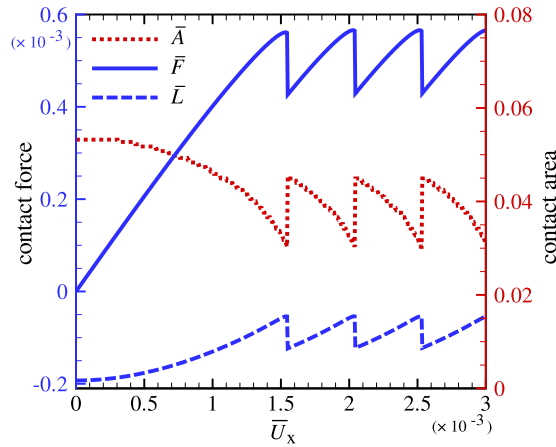


Fig. 6. Tangential and normal contact forces, \bar{F} and \bar{L} , and contact area \bar{A} with increasing tangential displacement \bar{U}_x . Results are shown for the normal displacement $\bar{\delta} = 0$ and $\bar{\phi}_n = \bar{\phi}_t = 2$.

Fig. 5 shows a monotonic reduction in $\langle \bar{F} \rangle$ with increasing E and/or decreasing τ_{\max} . An increase in E/τ_{\max} , corresponds to the CZM law describing linear elastic fracture mechanics behavior (Gao et al., 2003; Gao and Yao, 2004; Liu et al., 2015), with negligible adhesive behavior, and leads therefore to a negligible friction force, such that an ultra low friction regime is achieved (see Fig. 5).

3.2. Circular probe on flat body

Here, we perform simulations for adhesive frictional contact of a deformable solid with circular protrusion on a flat rigid substrate under mixed-mode loading. In this case, beside the tangential contact force, we also investigate the evolution of the normal contact force and focus on the change in the contact area.

The tangential contact force \bar{F} versus applied tangential displacement \bar{U}_x , for normal displacement $\bar{\delta} = 0$ and an interface with $\bar{\phi}_n = \bar{\phi}_t = 2$, is shown with the solid blue line in Fig. 6. In this figure, similar to the case of flat-on-flat contact in Section 3.1, a sawtooth curve for \bar{F} versus \bar{U}_x is observed due to the stick-slip motion. The evolution of the normal contact force \bar{L} is also included in Fig. 6 (see the dashed blue line). Here, the negative value of \bar{L} indicates tensile loading. This means that the summation of the attractive forces (with negative sign) on the interface is larger than the repulsive forces (with positive sign). By applying a larger $\bar{\delta}$ the solids are pushed harder against each other and the normal contact force \bar{L} may become positive (compressive loading).

Fig. 6 also presents the evolution of the contact area \bar{A} during tangential loading, shown by the dotted red line. During the sticking stages, a reduction in \bar{A} is observed with increasing \bar{U}_x , a behavior we refer to as “shear-peeling”. Subsequently, at the onset of sliding where the slip instability occurs, the contact area abruptly increases (reattachment). This cycle of area reduction \rightarrow slip instability \rightarrow reattachment persists for continued tangential displacement. The details of these events are examined in the following section.

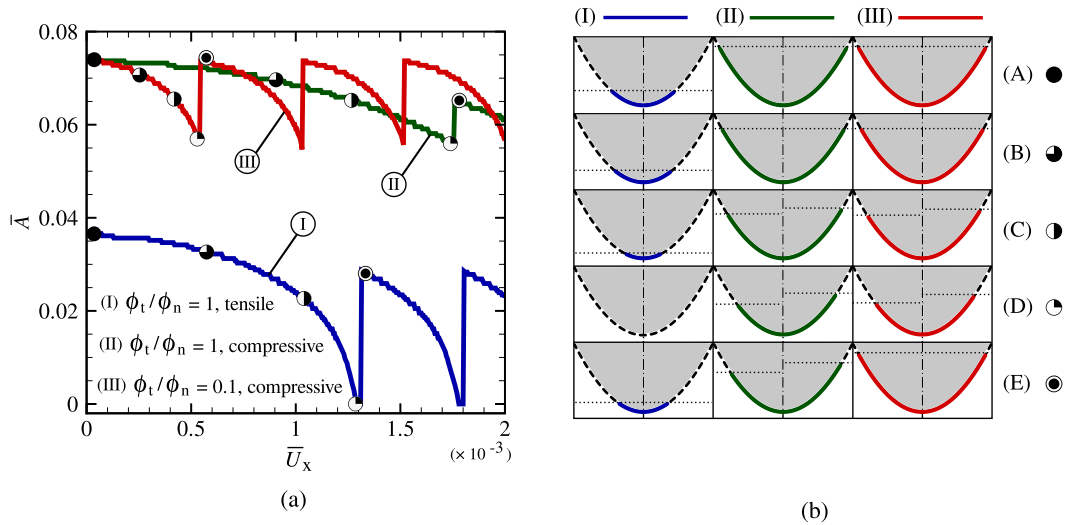


Fig. 7. (a) Contact area \bar{A} versus applied tangential displacement \bar{U}_x for different normal loading and ratio of tangential-to-normal work of separation. (b) Snapshots (A–E) of the contact region during tangential loading for the three cases shown in (a). Snapshots are denoted by the same symbols in both (a) and (b). Note that in (b), contact regions are shown in the original configuration. The horizontal dotted lines are a visual aid to distinguish between symmetry and asymmetry of the contact area. Results are shown for $\bar{\phi}_n = 2$.

3.2.1. Shear-peeling and reattachment

Waters and Guduru (2010) recorded images of the contact area evolution throughout their contact shearing experiments for a range of normal loads. Before the onset of sliding, these images demonstrated symmetric and asymmetric contact area reduction under tensile and compressive loading, respectively. After the onset of sliding, they could capture a partial reattachment under compressive loading. Here, we perform simulations with the aim of capturing these experimental features and to investigate whether the reattachment occurs also under tensile loading. Moreover, we also study the role of friction on the evolution of contact area.

Fig. 7a shows the evolution of the contact area \bar{A} versus the applied tangential displacement \bar{U}_x at various normal loadings, tensile and compressive, and the ratio of the tangential-to-normal work of separation, $\phi_t/\phi_n = 1$ and 0.1. For the chosen parameters in this figure, $\bar{\delta} \gtrsim 0.2$ and $\bar{\delta} < 0.2$ represent the compressive and tensile loading, respectively. Moreover, $\phi_t/\phi_n = 1$ and 0.1 are employed in order to investigate the role of high and low friction, respectively, on the contact area evolution: lowering the value of ϕ_t/ϕ_n , for example, resembles introducing lubricant into the interface.

Snapshots of the contact region, labeled as A–E, are shown in Fig. 7b for three cases in Fig. 7a at various values of the tangential displacement. These snapshots are denoted by the same symbols in both figures. In all cases, snapshot A is at $\bar{U}_x = 0$, B and C are during the shear-peeling stage, and D and E are before and after the first slip instability event. The following key features emerge from this figure:

- A \rightarrow B: The contact area shrinks symmetrically. This symmetrical peeling is observed in all cases: tensile/compressive loading and low/high friction.
- B \rightarrow C: Under tensile loading (case I), the contact area continues to shrink symmetrically. For compressive loading (case II and III), however, the contact area becomes asymmetric, with more peel occurring at the trailing edge of the contact than at the leading edge. The horizontal dotted lines are a visual aid to distinguish between symmetry and asymmetry of the contact area.
- C \rightarrow D: Under tensile loading in case I, a full separation occurs during tangential loading at the onset of sliding. On the contrary, for compressive loading (case II and III), there is no full separation and contact area continues to shrink asymmetrically.
- D \rightarrow E: As slip progresses within the contact area, slip instability occurs and immediately reattachment follows. Under tensile/compressive loading with high friction (case I and II), the reattachment occurs only partially. However, for the interface with low friction (case III), a full reattachment is observed (compare snapshots E and A).

The aforementioned features agree well with the experimental observations of Waters and Guduru (2010). Besides, two extra features are also captured compared to the experiments: First, the reattachment (D \rightarrow E) was not observed for tensile loading (case I) in the experiments. As mentioned in Waters and Guduru (2010), this might be because the employed feedback loop could not correct the normal loading fast enough to maintain contact as the slip instability occurred. Second, for the chosen material and interface properties only a *partial* reattachment was observed in the experiments. However, our results show that attaining a *full* reattachment is possible when friction is low (case III). In this case, as can be seen from the red line in Fig. 7a, the pre-sliding distance is small. Hence, the induced deformation in the solid during the sticking

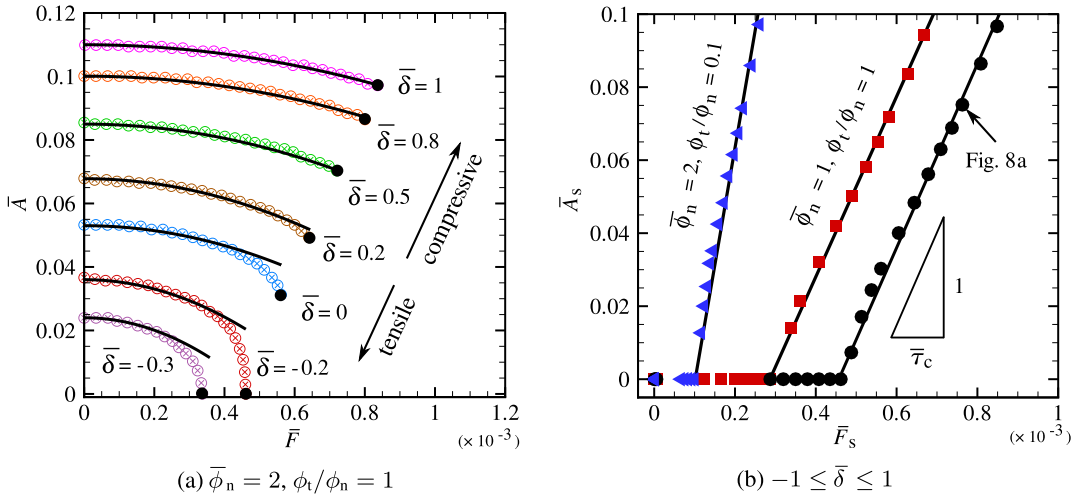


Fig. 8. (a) Contact area \bar{A} versus tangential contact force \bar{F} for various normal displacements $\bar{\delta}$. Solid curves are fits using Eq. (8) (Sahli et al., 2018). The filled circles indicate contact area \bar{A}_s at the maximum tangential contact force \bar{F}_s . (b) \bar{A}_s versus \bar{F}_s for the case shown in (a) along with cases for $\bar{\phi}_n = 1$, $\phi_t/\phi_n = 1$ and $\bar{\phi}_n = 2$, $\phi_t/\phi_n = 0.1$. Slopes of the solid lines in (b) represent the contact shear strength $\bar{\tau}_c$ (Sahli et al., 2018).

stage can be fully released as the slip instability occurs. Consequently, for the case of low friction, the initial configuration is re-attainable in the reattachment cycle.

3.2.2. Laws of area reduction and onset of sliding

A common way of identifying the law of contact area reduction is to plot the contact area \bar{A} as a function of the tangential contact force \bar{F} . To this end, the evolution of \bar{A} versus \bar{F} up to the onset of sliding for various normal displacements $\bar{\delta}$ is shown in Fig. 8a. For the chosen parameters in this figure, $\bar{\delta} \gtrsim 0.2$ and $\bar{\delta} < 0.2$ represent the compressive and tensile loading, respectively. It is observed that for all $\bar{\delta}$, the initial contact area $\bar{A}_0 = \bar{A}(\bar{U}_x = 0)$ decreases until a maximum \bar{F} is reached at the onset of sliding.

Recently, Sahli et al. (2018) carried out sliding experiments for a range of compressive loadings. In their experiments, for both smooth and rough asperities, the reduction in the contact area was found to be well fitted by an empirical quadratic law of the form:

$$\bar{A} = \bar{A}_0 - \zeta \bar{F}^2, \tag{8}$$

with ζ being a fitting parameter. We have fitted this equation to our results for adhesive frictional contact of a smooth asperity with various normal displacements $\bar{\delta}$, see the solid curves in Fig. 8a. It is observed that a good agreement is obtained for compressive loading, similar to the experiments in Sahli et al. (2018). For tensile loading, for which experimental data is not available, we find a deviation from the quadratic law of Eq. (8). It is concluded that under tensile loading, when the onset of sliding is approached, the rate of contact area reduction increases.

In Fig. 8a, filled black circles indicate contact area \bar{A}_s at the maximum tangential contact force \bar{F}_s just before the onset of sliding, i.e., the static friction force. Fig. 8b illustrates the data points (\bar{A}_s, \bar{F}_s) related to various $\bar{\delta}$ for the case shown in Fig. 8a ($\bar{\phi}_n = 2$, $\phi_t/\phi_n = 1$) along with two other cases where $\bar{\phi}_n$ and ϕ_t/ϕ_n are independently varied. Interestingly, in all cases, the points marking the onset of sliding (\bar{A}_s, \bar{F}_s) align well on a straight line. This shows that,

$$\bar{F}_s = \bar{\tau}_c \bar{A}_s + \bar{F}_{s,nc}, \tag{9}$$

with $\bar{\tau}_c$ and $\bar{F}_{s,nc}$ being the contact shear strength and the maximum sliding force without contact (i.e. without a contact area under repulsion), respectively. The linear relation in Eq. (9) is in line with the so-called threshold law by Sahli et al. (2018). Since Sahli et al. (2018) only considered compressive loading, they concluded that the straight line goes through the origin. Here, by considering also tensile loading, we can observe cases where \bar{A}_s is zero at a finite value of tangential contact force due to the adhesive interactions at the interface. For example, in Fig. 8a, this is the case for the normal displacements $\bar{\delta} = -0.2$ and -0.3 . This behavior can be better captured by our proposed ‘extended threshold law’ (Eq. (9)), choosing this name is inspired by the extended Amontons’ law, which incorporates similarly an adhesive contribution.

Finally, Fig. 8b shows that the contact shear strength $\bar{\tau}_c$ and the sliding force when there is no repulsive contact area $\bar{F}_{s,nc}$ change with interfacial properties, namely $\bar{\phi}_n$ and ϕ_t/ϕ_n . The following key features are identified:

- Decreasing the normal work of separation decreases $\bar{F}_{s,nc}$, yet it has negligible effect on $\bar{\tau}_c$. This can be seen from Fig. 8b, by comparing the lines marked with black circles for $\bar{\phi}_n = 2$ and red squares for $\bar{\phi}_n = 1$. A way to reduce $\bar{\phi}_n$ is the immersion of the surface in ethanol or salt solution (Gao et al., 2004).

- Decreasing the ratio of tangential-to-normal work of separation results in smaller values of $\bar{F}_{s,nc}$ and $\bar{\tau}_c$. This is observed from Fig. 8b, by comparing the lines marked with black circles for $\phi_t/\phi_n = 1$ and blue triangles for $\phi_t/\phi_n = 0.1$ (in both cases $\phi_n = 2$). The value of $\bar{\phi}_t$ can be reduced by introducing a lubricant into the interface.

4. Concluding remarks

A simple computational model is developed to study adhesive frictional contacts of elastically deformable solids under mixed-mode loading. The strength of the model lies in its capability of studying the variation of contact area and of the friction force before and after the onset of sliding, under a compressive or tensile loading. The full range of conditions is difficult to be addressed experimentally.

The simulations are performed for an elastically deformable adhesive circular protrusion sliding against a rigid flat. The model can capture the features observed in the experiments by Waters and Guduru (2010) and by Sahli et al. (2018):

- Under compressive loading, a tangential displacement, first induces the contact area to shrink symmetrically. As the applied tangential displacement increases more peel occurs at the trailing edge. Under tensile loading, on the contrary, the contact area continues to shrink symmetrically.
- Reduction in the contact area as a function of the tangential contact force is found to be well fitted by the empirical quadratic law reported in Sahli et al. (2018) for experimental results under compressive loading. Moreover, there is a linear relation between the maximum tangential contact force at the onset of sliding and its corresponding contact area at various normal loadings.

In addition the model can predict the following behavior, not yet observed experimentally:

- With slip instabilities occurring during sliding, a cycle of contact area reduction and reattachment persists for continued tangential loading, even under tension. Whether the reattachment is partial or full depends on friction: The lower the friction, the more complete the reattachment.
- Under tensile loading the empirical quadratic law relating area to tangential force breaks down: there is a larger rate of contact area reduction when the onset of sliding is approached.
- Also under tensile loading a linear relation holds between the maximum tangential contact force at the onset of sliding and the corresponding contact area. However, under tensile loading, a full interface separation can take place at the onset of sliding with a non-zero tangential force: The contact area is under adhesive contact.

Acknowledgments

LN received funding from the European Research Council (ERC) under the European Unions Horizon 2020 research and innovation programme (grant agreement no. 681813). LN also acknowledges support by the Netherlands Organisation for Scientific Research NWO and Dutch Technology Foundation STW (VIDI grant 12669).

Supplementary material

Supplementary material associated with this article can be found, in the online version, at doi:10.1016/j.jmps.2019.06.010.

References

- Adams, G.G., 2014. Stick, partial slip and sliding in the plane strain micro contact of two elastic bodies. *R. Soc. Open Sci.* 1 (3), 140363.
- Barthel, E., Haiat, G., 2002. Approximate model for the adhesive contact of viscoelastic spheres. *Langmuir* 18 (24), 9362–9370.
- Chen, S., Wang, T., 2006. General solution to two-dimensional nonslipping JKR model with a pulling force in an arbitrary direction. *J. Colloid Interface Sci.* 302 (1), 363–369.
- Ciavarella, M., 2018. Fracture mechanics simple calculations to explain small reduction of the real contact area under shear. *Facta Univ. Ser.* 16 (1), 87–91.
- Derjaguin, B.V., Muller, V.M., Toporov, Y.P., 1975. Effect of contact deformations on the adhesion of particles. *J. Colloid Interface Sci.* 53 (2), 314–326.
- Dikken, R.J., Thijssen, B.J., Nicola, L., 2017. Friction of atomically stepped surfaces. *Phys. Rev. B* 95 (10), 104106.
- Gao, H., Ji, B., Jäger, I.L., Arzt, E., Fratzl, P., 2003. Materials become insensitive to flaws at nanoscale: lessons from nature. *Proc. Natl. Acad. Sci.* 100 (10), 5597–5600.
- Gao, H., Yao, H., 2004. Shape insensitive optimal adhesion of nanoscale fibrillar structures. *Proc. Natl. Acad. Sci.* 101 (21), 7851–7856.
- Gao, Y., Luedtke, W., Gourdon, D., Ruths, M., Israelachvili, J., Landman, U., 2004. Frictional forces and Amontons' law: from the molecular to the macroscopic scale. *J. Phys. Chem. B* 108 (11), 3410–3425.
- Gao, Y., 2010. A Peierls perspective on mechanisms of atomic friction. *J. Mech. Phys. Solids* 58 (12), 2023–2032.
- Greenwood, J., Johnson, K., 1998. An alternative to the Maugis model of adhesion between elastic spheres. *J. Phys. D* 31 (22), 3279.
- Huang, G.-Y., Yan, J.-F., 2017. A mechanical model for the adhesive contact with local sliding induced by a tangential force. *Acta Mech. Solida Sin.* 30 (4), 369–373.
- Johnson, K.L., 1997. Adhesion and friction between a smooth elastic spherical asperity and a plane surface. *Proc. R. Soc. Lond. A* 453, 163–179.
- Johnson, K.L., Kendall, K., Roberts, A., 1971. Surface energy and the contact of elastic solids. *Proc. R. Soc. Lond. A* 324, 301–313.
- Khajeh Salehani, M., Irani, N., Müser, M., Nicola, L., 2018. Modelling coupled normal and tangential tractions in adhesive contacts. *Tribol. Int.* 124, 93–101.
- Krylov, S.Y., Frenken, J.W., 2014. The physics of atomic-scale friction: basic considerations and open questions. *Phys. Status Solidi (b)* 251 (4), 711–736.
- Liu, Y., Liu, H., Gao, Y., 2015. Can mushroom-shaped fibers enhance the bio-adhesive performance? *J. Mech. Med. Biol.* 15 (05), 1550068.
- Maugis, D., 1992. Adhesion of spheres: the JKR-DMT transition using a Dugdale model. *J. Colloid Interface Sci.* 150 (1), 243–269.
- McGarry, J.P., Máirtín, É.Ó., Parry, G., Beltz, G.E., 2014. Potential-based and non-potential-based cohesive zone formulations under mixed-mode separation and over-closure. Part i: theoretical analysis. *J. Mech. Phys. Solids* 63, 336–362.

- Mergel, J.C., Sahli, R., Scheibert, J., Sauer, R.A., 2018. Continuum contact models for coupled adhesion and friction. *J. Adhes.* 0 (0), 1–33.
- Prodanov, N., Dapp, W.B., Müser, M.H., 2014. On the contact area and mean gap of rough, elastic contacts: dimensional analysis, numerical corrections, and reference data. *Tribol. Lett.* 53 (2), 433–448.
- Sahli, R., Pallares, G., Ducottet, C., Ali, I.B., Al Akhrass, S., Guibert, M., Scheibert, J., 2018. Evolution of real contact area under shear and the value of static friction of soft materials. *Proc. Natl. Acad. Sci.* 115 (3), 471–476.
- Savkoor, A., Briggs, G., 1977. The effect of tangential force on the contact of elastic solids in adhesion. *Proc. R. Soc. Lond. A* 356, 103–114.
- Socoliuc, A., Bennewitz, R., Gnecco, E., Meyer, E., 2004. Transition from stick-slip to continuous sliding in atomic friction: entering a new regime of ultralow friction. *Phys. Rev. Lett.* 92 (13), 134301.
- Spence, D., 1968. Self similar solutions to adhesive contact problems with incremental loading. *Proc. R. Soc. Lond. A* 305, 55–80.
- Sun, Y., Beltz, G.E., Rice, J.R., 1993. Estimates from atomic models of tension-shear coupling in dislocation nucleation from a crack tip. *Mater. Sci. Eng.* 170 (1–2), 67–85.
- Thornton, C., 1991. Interparticle sliding in the presence of adhesion. *J. Phys. D* 24 (11), 1942.
- Van den Bosch, M., Schreurs, P., Geers, M., 2006. An improved description of the exponential Xu and Needleman cohesive zone law for mixed-mode decohesion. *Eng. Fract. Mech.* 73 (9), 1220–1234.
- Venugopalan, S.P., Nicola, L., Müser, M.H., 2017. Green's function molecular dynamics: including finite heights, shear, and body fields. *Model. Simul. Mater. Sci. Eng.* 25 (3), 034001.
- Waters, J.F., Guduru, P.R., 2010. Mode-mixity-dependent adhesive contact of a sphere on a plane surface. *Proc. R. Soc. Lond. A* 466, 1303–1325.
- Xu, X.-P., Needleman, A., 1993. Void nucleation by inclusion debonding in a crystal matrix. *Model. Simul. Mater. Sci. Eng.* 1 (2), 111.